SUPPLEMENTARY INFORMATION

Characterization of Rac1 constructs

Using a pull down assay with PAK, a Rac effector, as bait we examined how truncations of Rac or the Jα helix (Jα 539-547, Rac 2-4, Fig. S1a,b) impacted Rac-PAK interaction. Connecting Jα Leu546 to Rac Ile4 led to a substantial reduction in effector binding, indicating that this construct is capable of inhibiting Rac activity. The angle between the LOV domain and Rac is also important (Fig. S1a): Substitution of Leu546 by proline (L546P) negated the caging effect, and further reduction of PAK binding was achieved by including rigid structural motifs such as Schellman α-Caps to transition the Jα helix into the first β-strand of Rac at fixed angles (Fig. S1b), although efficient uncaging of the Schellman caps could not be achieved (data not shown). The LOV546-Rac4 construct induced ruffling, a phenotype of Rac overexpression in living cells. This was likely due to activation of endogenous Rac1 through sequestration of negative regulatory GAP proteins, as coexpression of dominant-negative Rac1 (T17N) reduced the ruffling (data not shown). This was eliminated by including the E91H and N92H mutations, described below (Fig. S2). The Q61L mutation used in PA-Rac1 is known to block GEF and GDI binding[25,26].

Crystal structures of PA-Rac1

The dark state structures of PA-Rac1 and of the C450A and C450M mutants were determined to a resolution of 1.9, 1.6 and 2.2 Å, respectively (see Table S2). The two mutant structures adopt the same fold as the PA-Rac1 protein with an RMSD of 0.21 Å (C450A) and 0.35 Å (C450M) for all Cα atoms. In all structures the effector loop of the Rac1 domain (residues 30-40 of Rac1) is less well defined but the major conformation was built in these models. The solvent accessible side chain of Cys105 located at the end of helix H3 of Rac1 shows additional density in the PA-Rac1 structure arising from a possible modification with DTE but no clear conformation could be included in the structure. Despite a small movement (0.4-0.6 Å) of residues 449-451 to accommodate the larger side chain in the C450M mutant the FMN binding site is identical in all three structures. Similar to the structure of the isolated LOV domain (PDB code 2V0U), Cys450 of PA-Rac1 adopts a double conformation in the dark state and forms no covalent bond to the FMN. The Cε atom of the side chain of the methionine in C450M is in close proximity to the isoalloxazine ring of FMN but does not form a covalent adduct in the dark state.

The connection between the two individual domains, including the Jα helix of LOV2 and the S1 strand of Rac1, is well defined in the electron density. Both domains adopt their previously reported folds (rmsd = 0.54 Å, PA-Rac1 Lov2 domain compared to 2V0U; RMSD = 0.73 Å, PA-Rac1 Rac1 domain compared to 1MH1) and inherit their natural ligands FMN and GTP/Mg^{2+} respectively. The interface between the two domains comprises a total buried surface area of 840 $Å^2$ for each domain. Rac1 interfacing residues are located mainly in secondary structural elements including strands 1-4, helix 1 and the 3_{10} helix around Pro 69 of Rac1, whereas the interfacing residues of LOV2 are located in the loop regions between strands Aβ and Bβ, Hβ and Iβ, and helices Dα and the neighbouring loop to helix Eα as well as the C-terminal part of the Jα helix. Compared to 2V0U the N-terminal helix Aα is less pronounced. Residues 403-407 of LOV2 cannot adopt the conformation seen in 2V0U since they would clash with the Rac1 domain of PA-Rac1. These residues are rotated around 180° at Leu408 and are pointing in the direction of the Jα helix.

Structural Modelling

One striking result from our study is that the caging of Rac1 is very sensitive to the length of the linker that connects Rac1 to LOV2. Adding or removing a single residue from the linker disrupts caging (Fig. S1a). To determine the physical basis for this length dependence we performed structure prediction simulations with the Rosetta molecular modelling program on three of the constructs (545-4, 546-4, 547-4) used in the dark state pull down experiments. The most prevalent conformation of 546-4 was similar to the crystal structure of 546-4 and contains an extensive interface between Rac1 and LOV2 that is predicted to occlude CRIB binding. A similar interface was not observed in the low energy conformations predicted for 545-4 and 547-4, and the binding site for CRIB is predicted to be accessible in the majority of the low energy conformations.

Models of the dark state 546-4 structure showed a marked difference in quaternary structure from models of 545-4 and 547-4, and importantly, were similar to the crystal structure of PA-Rac1 (Figs. S10-13, Tables S3-5). Our lowest RMSD model was 1.7 Å away from the solved crystal structure. Furthermore, the largest cluster of 546-4 models was on average 4.5 Å RMSD away from the solved crystal structure. As in the crystal structure, a well-packed binding interface was formed between the two domains. Residues Leu422, Pro423, Ile428, Tyr508, Leu546 from LOV2 as well as Phe37 and Trp56 of the beta sheet from Rac1 created hydrophobic contacts across the LOV2-Rac1 interface. Residues Asp419 and Trp56 also made a hydrogen bond across the interface. The tight packing of the Rac1 β strand against LOV2 occluded the strand addition binding of CRIB to the Rac1 β sheet.

An interface did not form in models of the 545-4 construct (Fig. S12). In these models, Rac1 orients away from the LOV2 domain, and thus CRIB is not occluded from binding LOV2-Rac1. Also, a LOV2-Rac1 interface did not form in most of the models of the 547-4 construct (Fig. S13). Clusters generated using the 547-4 simulations contained less models per cluster than all other simulations. Because of the longer linker, 547-4 could sample more conformational space. In the majority of conformations the Rac1 β-sheet was not adjacent to the LOV2 domain and the CRIB domain binding site was predicted to be accessible.

Isothermal Titration Calorimetry

Isothermal titration experiments were performed to analyze the ability of lit as well as dark state 546-4 to bind the CRIB domain of PAK1. The lit state mimetic, I539E, of 546-4 bound to PAK1 CRIB with an affinity of 220-280 nM. In contrast, the dark state C450A 546-4 mimetic bound PAK1 CRIB with a ten-fold weaker affinity of 2.3-3.1 μM (Table S1 and Fig. S3).

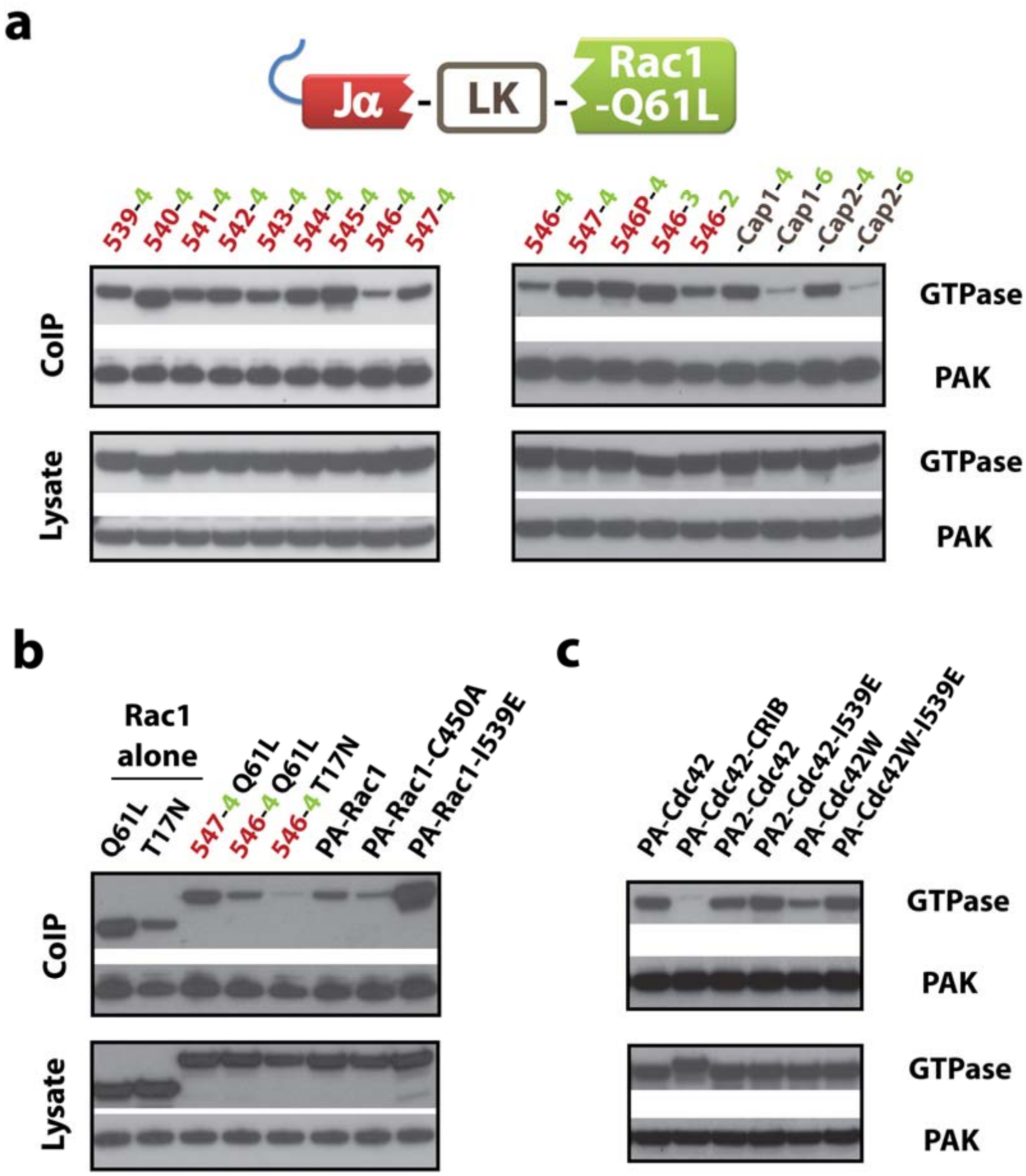

Figure S1. Screening of PA-Rac1 and PA-Cdc42 in PAK pull-down experiments. **a-b,** Screening PA-Rac constructs by co-immunoprecipitation with PAK in the dark. *539-547 (red)* indicates the terminal amino acid residue of the Jα; *4-2 (green)* indicates the starting residue of Rac1; Cap1 and 2 (gray) are inserted Schellman cap linkers; PA-Rac1 = 546-4 Q61L/E91H/N92H; -*C450A* = light-insensitive mutant of PA-Rac1; -*I539E* = lit state mutant of PA-Rac1. **c,** engineering of PA-Cdc42. PA-Cdc42 = 546-4 fusion of LOV and Cdc42; CRIB = control in which the CRIB sequence from PAK was linked to PA-Cdc42; PA2-Cdc42 = 546-4/E518R/V520F/A524D; PA-Cdc42W = 546-4/F56W.

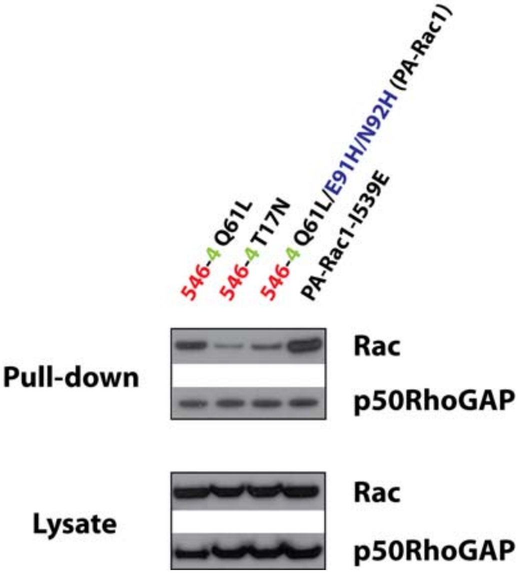

Figure S2. Point mutations that disrupt Rac-GAP interactions. The indicated PA-Rac1 constructs were coexpressed with Myc-tagged p50RhoGAP in HEK293 cells in the dark. Co-immunoprecipitation indicated that the 546-4/Q61L construct interacts strongly with p50RhoGAP in the dark, consistent with its induction of ruffles in living cells due to sequestration of GAP proteins. The switch I and II and the α3 helix of Rho GTPases have been shown to interact with Rho GAP proteins[27,28]. Because the switch I and II region of Rac1 are critical for interactions with effectors, GAP interactions were blocked by introducing two point mutations in the α3 helix (E91H/N92H, *blue*) to specifically disrupt the interactions of Rac1 with GAP proteins. The binding of PA-Rac1 to p50RhoGAP in the dark is substantially decreased compared to that of the 546-4/Q61L construct. Although the lit state mutant (I539E) of PA-Rac1 restored GAP binding, indicating that the E91H/N29H mutations cannot effectively block GAP binding when the switch regions are exposed, effector binding remains intact and may outcompete GAP interaction.

Table S1. ITC experiments titrating PAK1 CRIB with dark or lit state mutants of PA-Rac1 (Two experiments are shown per mutant).

Experiment	K_d (μM)	ΔH (Kcal mol^{-1})	ΔS (Kcal mol^{-1} K^{-1})	N
C450A *(dark state)*	2.3 ± 0.43	$-7.0\times10^{3} \pm 490$	2.6	1.0 ± 0.051
	3.1 ± 1.3	$-5.6\times10^{3} \pm 1900$	6.6	0.64 ± 0.18
I539E *(lit state)*	$2.2\times10^{-1} \pm 1.5\times10^{-2}$	$-1.8\times10^{4} \pm 160$	-30.0	0.95 ± 0.0057
	$2.8\times10^{-1} \pm 4.3\times10^{-2}$	$-1.8\times10^{4} \pm 360$	-31	0.95 ± 0.013

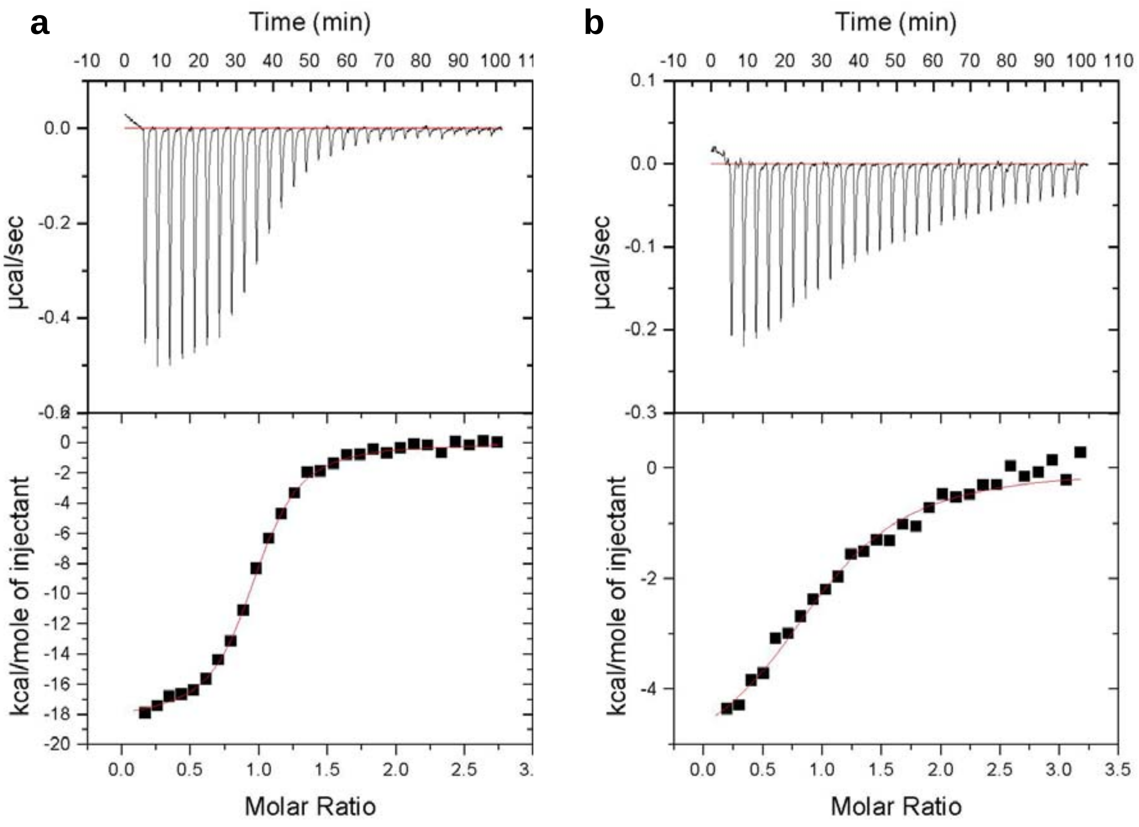

Figure S3. Binding of CRIB domain of PAK1 to the dark and lit state mutant of PA-Rac1 in isothermal titration calorimetry. The CRIB domain of PAK1 was titrated with either the lit (**a**, I539E) or dark (**b**, C450A) mutant of PA-Rac1. The raw data of heat generated per injection is shown in the top panel, and integrated data of heat output per mole of injected PA-Rac1 mutant versus molar ratio of PA-Rac1 mutant to CRIB is shown at the bottom. **a**, lit state mutant (I539E): $K_d = 2.2\text{x}10^{-1} \pm 1.5\text{x}10^{-2}$ µM, N= $0.95 \pm 5.7\text{x}10^{-3}$; **b**, dark state mutant (C450A): $K_d = 2.3 \pm 0.43$ µM, N= $1.0 \pm 5.1\text{x}10^{-2}$.

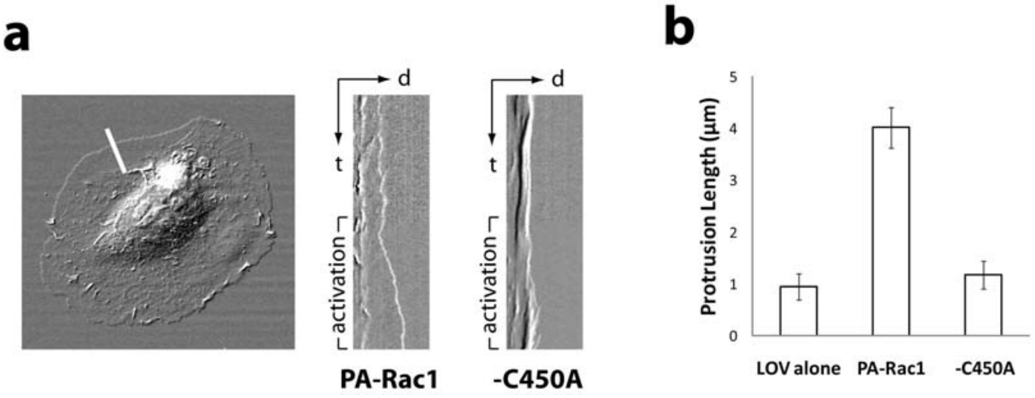

Figure S4. Whole-cell irradiation of PA-Rac1 induces protrusion. a, Kymograph analyses comparing protrusion of HeLa cells expressing PA-Rac1, its C450A mutant, and the LOV domain alone. **b**, Cells were irradiated for 5 minutes at 515 nm (a wavelength not affecting LOV) followed by 5 min at the activating wavelength of 458 nm. The maximum increase in kymograph width over the average width prior to 515 nm irradiation was recorded for >104 kymographs and >14 cells per bar. Protrusions induced by PA-Rac1 were more than 4 times as long as those from controls (short axis of kymograph = 20 μm).

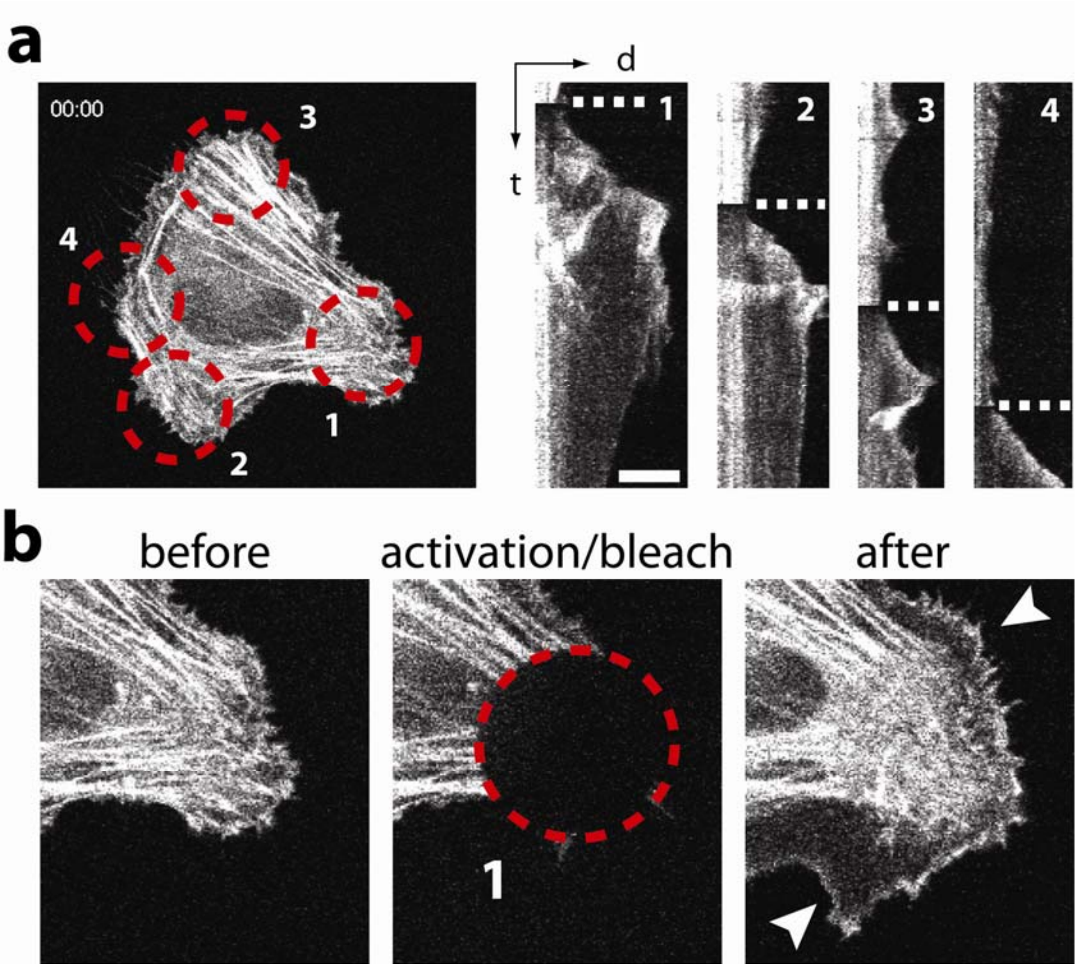

Figure S5. Actin reorganization induced by PA-Rac1 activation. a, A HeLa cell coexpressing mCherry-tagged PA-Rac1 and mVenus-tagged actin was sequentially irradiated at four different positions, each time in a 20 μm diameter spot with both 458 nm light to activate PA-Rac and 515 nm light to bleach the actin (*left,* also see Supplementary Movie S3). Kymograph analyses of mVenus fluorescence were performed on line scans perpendicular to the cell edge in each irradiated region (*right*). White dotted lines indicate the time of irradiation for each spot. The kymographs showed induction of protrusion and rapid recovery of actin at the cell borders. **b**, Fluorescence images of mVenus-actin are shown before and after irradiation of the first spot. The two arrows indicate the accumulation of actin at the leading edge (bar = 10 microns, representative data from analysis of 3 cells, 9 spots).

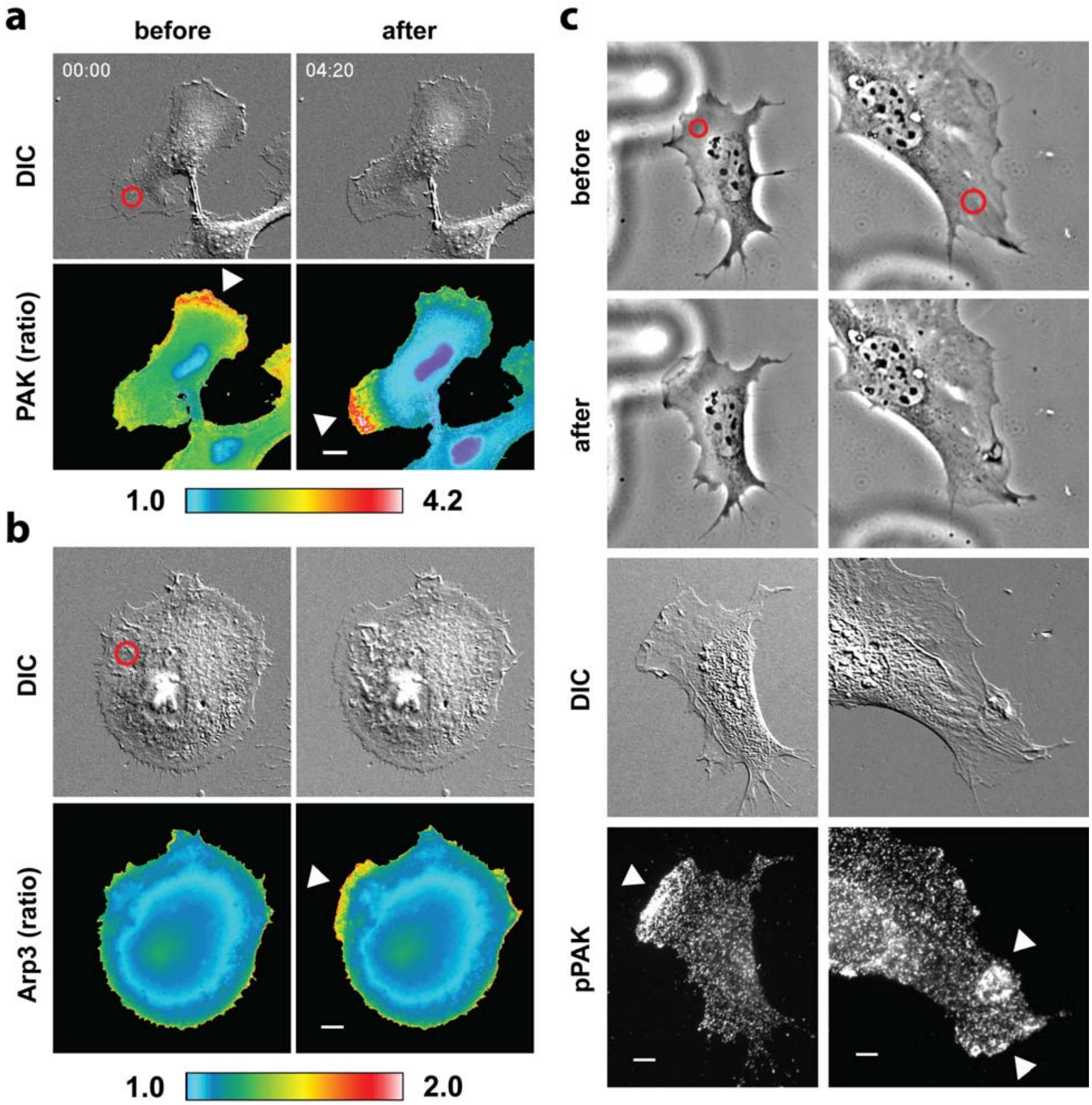
a
before
after
00:00
04:20
DIC
PAK (ratio)
1.0
4.2
b
DIC
Arp3 (ratio)
1.0
2.0
c
before
after
DIC
pPAK

Figure S6. Activation of PA-Rac induces translocation of PAK, translocation of Arp3, and local phosphorylation of PAK. **a**, HeLa cells coexpressing mCerulean-PA-Rac, mVenus-PAK and mCherry (as a volume indicator) were locally irradiated at 473 nm to generate protrusions (red circle, DIC). The ratio images of mVenus-PAK over mCherry before and after irradiation, indicative of PAK localization, are shown in pseudocolor (ratio). The arrows point to accumulation of PAK at constitutive ruffles (left) and translocation of PAK to the protrusion induced by PA-Rac (right). 10 additional examples are presented in Supplementary Movie S4. **b**, Translocation of Arp3 was investigated as above using mVenus-Arp3 (n = 3). **c**, MEF cells expressing mVenus-PA-Rac were plated onto etched grid coverslips and locally irradiated at 473 nm (red circle) to generate protrusion (phase-contrast images shown before and after irradiation). The cells were immediately fixed and stained for phospho-PAK. The numbers on the etched grids were used to locate irradiated cells after fixation (DIC). The acute staining of phospho-PAK (arrows) at PA-Rac induced protrusions and dorsal ruffles indicates local PAK activation (pPAK). Scale bars, 10 µm.

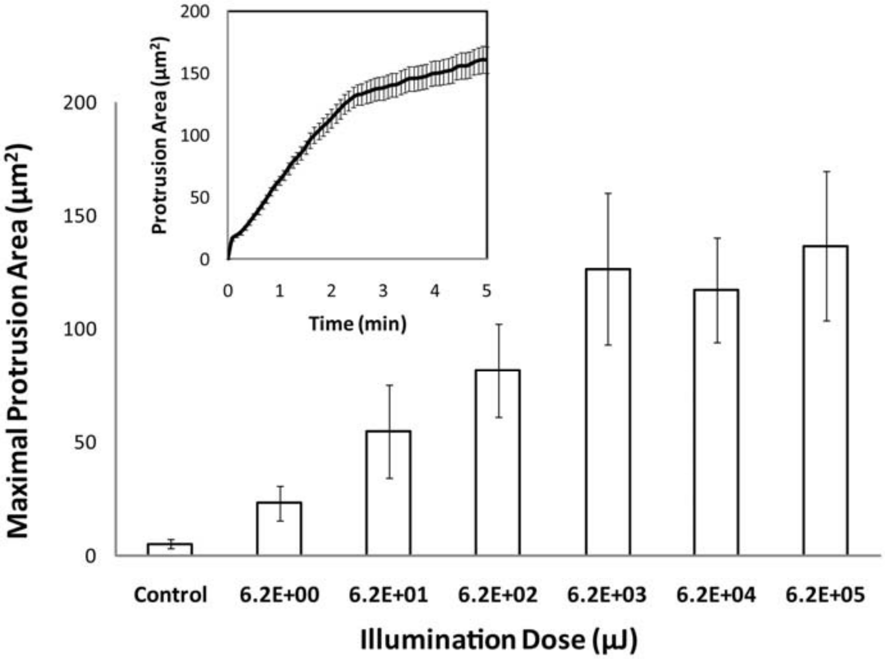

Figure S7. Dose-dependent induction of protrusion in MEF cells expressing PA-Rac1. MEF cells expressing mVenus-tagged PA-Rac1 were irradiated in a 10 µm spot with 458 nm laser at the light dose indicated. The lowest dose corresponds to 0.1% of laser power with 10 µs exposure time. Protrusion maps showed extension followed by retraction within 2.5 minutes at all the displayed doses. The maximum area reached within 2.5 minutes was plotted as a function of light dose. This plateaued at 6.2 x 10^3 µJ, reaching a maximal size of 125 µm^2. The kinetics of protrusion were remarkably constant, as shown in the inset detailing protrusions for the 6.2 x 10^3 µJ setting. Data are presented as means +/- 95% confidence intervals (n = 25~50 cells for each power setting and n = 50 cells for the inset).

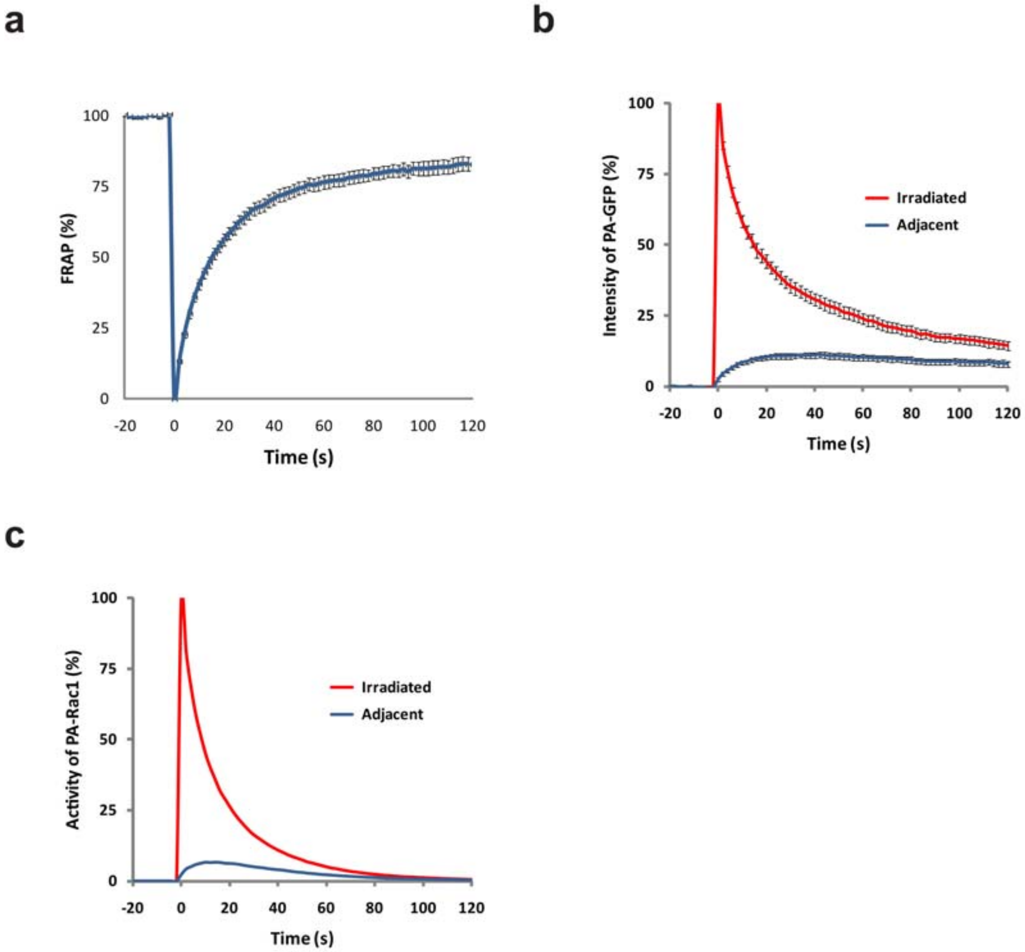

Figure S8. FRAP, PA-GFP tracking and decay of PA-Rac1 activity. a, MEF cells expressing PA-Rac1 tagged with mVenus were bleached for 10 μs at 515 nm in a 10 μm spot. The recovery of mVenus fluorescence within the bleached region was monitored at 2s intervals and the normalized intensity (based on the whole cell average intensity) is presented. **b**, MEF cells expressing PA-Rac1 tagged with PA-GFP were irradiated for 10 μs at 405 nm in a 10 μm spot. Fluorescence images (excitation 488 nm) of PA-GFP were then acquired at 2s intervals in the irradiated spot and a contiguous spot of equal size. The figure shows average intensities in the adjacent and irradiated spots, both normalized to the initial intensity of the irradiated spot (means +/- 95% confidence intervals). **c**, The dark recovery rate of PA-Rac1 at room temperature was obtained as previously described[5] ($t_{1/2}$ = 43 s). This decay rate (which is likely faster at 37C) was used to compute the level of active species present in each spot over time (exponential decay of the concentrations indicated in panel a). The curves show the estimated relative activities in the two adjacent regions, irradiated and nonirradiated.

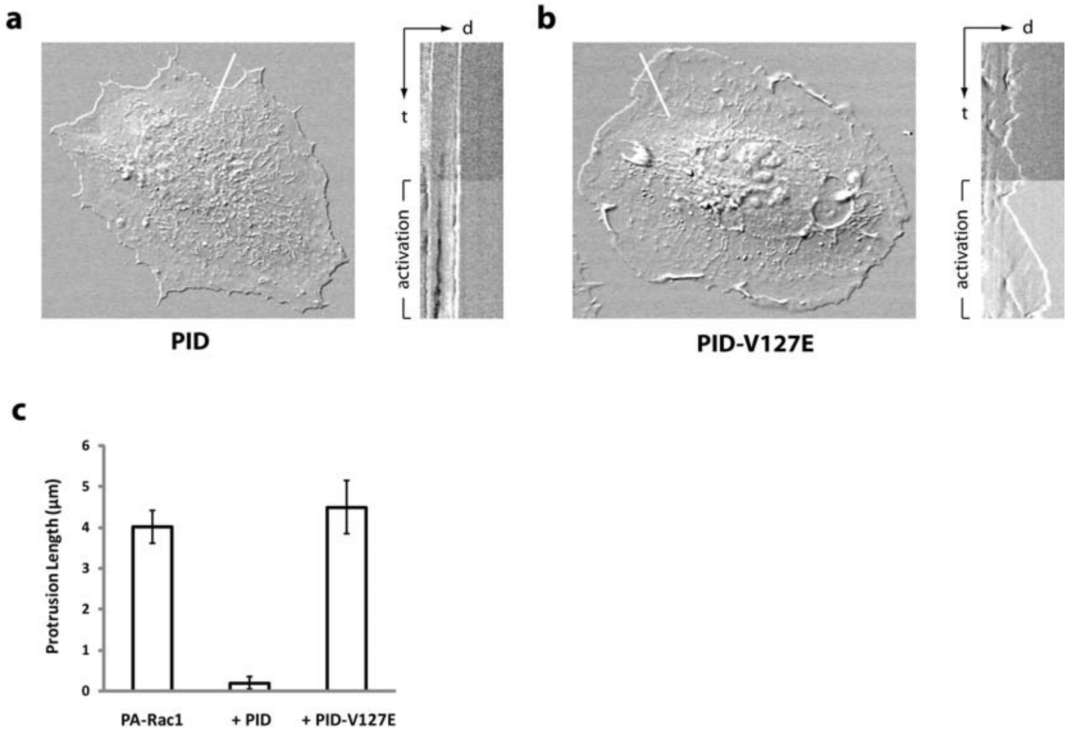

Figure S9. The kinase activity of PAK is important for Rac1-induced ruffling and protrusion. The mVenus-tagged PA-Rac1 and mCherry-tagged PAK inhibitory domain[29] (PID, **a**) or a mutant defective in Pak binding (PID-V127E, **b**) were coexpressed in HeLa cells. The cells were irradiated for 5 minutes at 515 nm (a wavelength not affecting LOV) followed by 5 min at the activating wavelength of 458 nm. The DIC images of the cells after 458 nm irradiation are shown (*left*, **a** and **b**). Kymograph analyses (*right*, **a** and **b**) were performed on 112 lines from 14 cells. The protrusions were abolished in cells co-expressing PID (**c**), whereas expression of the PID mutant resulted in an average protrusion length indistinguishable from those of the cells expressing PA-Rac1 alone. (means +/- 95% confidence intervals, short axis of kymograph = 20 µm).

Table1. S2 X-ray diffraction data processing and refinement statistics.

Data collection	**WT**	**C450A**	**C450M**
Resolution Range (Å)	50-1.9 (1.95-1.9)	50-1.6 (1.65-1.60)	50-2.2 (2.3-2.2)
Space group	$P3_221$	$P3_221$	$P3_221$
Unit cell parameter (Å)	**a**=**b**=113.88, **c**= 69.52	**a**=**b**=112.64, **c**= 69.31	**a**=**b**=112.39, **c**= 69.20
No. of Reflections	239280	1027560	95378
Completeness (%)	99.8 (99.6)	99.8 (99.5)	99.5 (99.8)
Redundancy	5.8 (5.8)	15.4 (12.3)	3.7 (3.7)
Rmerge (%)	6.7 (54.5)	6.5 (45.4)	10.7 (49.9)
Mean I/(σ)I	19.1 (3.7)	26.2(5.8)	11.7 (2.6)
Wilson B factor (Å^2)	20.6	18.8	22.7

Refinement			
Resolution (Å)	40-1.9 (1.94-1.9)	40-1.6 (1.63-1.60)	40-2.2 (2.28-2.2)
Rwork (%)	16.7 (21.5)	16.9 (19.1)	18.6 (22.5)
Rfree (%)	19.5 (27.7)	18.7 (21.0)	22.6 (30.4)
R.m.s.d. bond lengths (Å)	0.009	0.009	0.006
R.m.s.d. bond angles (°)	1.2	1.3	1.032
No. protein atoms	2608	2606	2523
No. of ligand atoms	63	75	62
No. of Mg^{2+} / Ca^{2+} / Cl^- atoms	1/1/0	1/0/3	1/0/2
No. of Solvent molecules	313	396	214
Average B factor, protein atoms, (Å^2)	23.3	21.4	22.0
Average B factor, ligands (Å^2)	18.0	18.2	19.6

Average B factor, solvent (Å^{2})	33.3	36.2	27.3
Maximum likelihood based coordinate error (Å)	0.23	0.18	0.26
Ramachandran Plot			
Favored regions (%)	98.1	98.7	98.4
Allowed regions (%)	1.9	1.3	1.6
Disallowed regions (%)	0	0	0

*Numbers in parentheses are for the highest resolution shell

The structural coordinates of PA-Rac1 and its mutants have been submitted to the Protein Data Bank under accessions 2wkp (WT), 2wkq (C450A) and 2wkr (C450M).

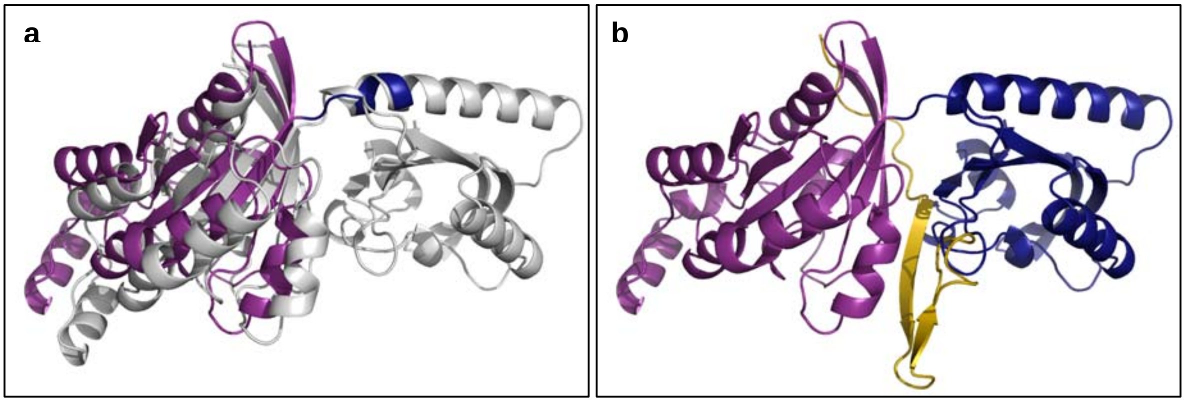

Figure S10. **a,** Superposition of the X-ray structure of PA-Rac1 (*gray*) and the 546-4 model with the lowest RMSD to the X-ray structure. LOV2 is in *blue*, and Rac1 in *purple*. **b,** The model with the lowest RMSD to the PA-Rac1 X-ray structure is unable to bind the CRIB domain (*yellow*).

Table S3. Simulations of 546-4 LOV2-Rac1 Construct

Cluster Number	Members	Score[1]	RMSD from X-ray (Å)	Binds CRIB?
1	566	-512	4.5	No
2	151	-512	2.1	No
3	62	-513	7.6	Yes
4	60	-506	4.5	No
5	54	-503	9.0	Yes

[1] Average of 10% best scoring decoys

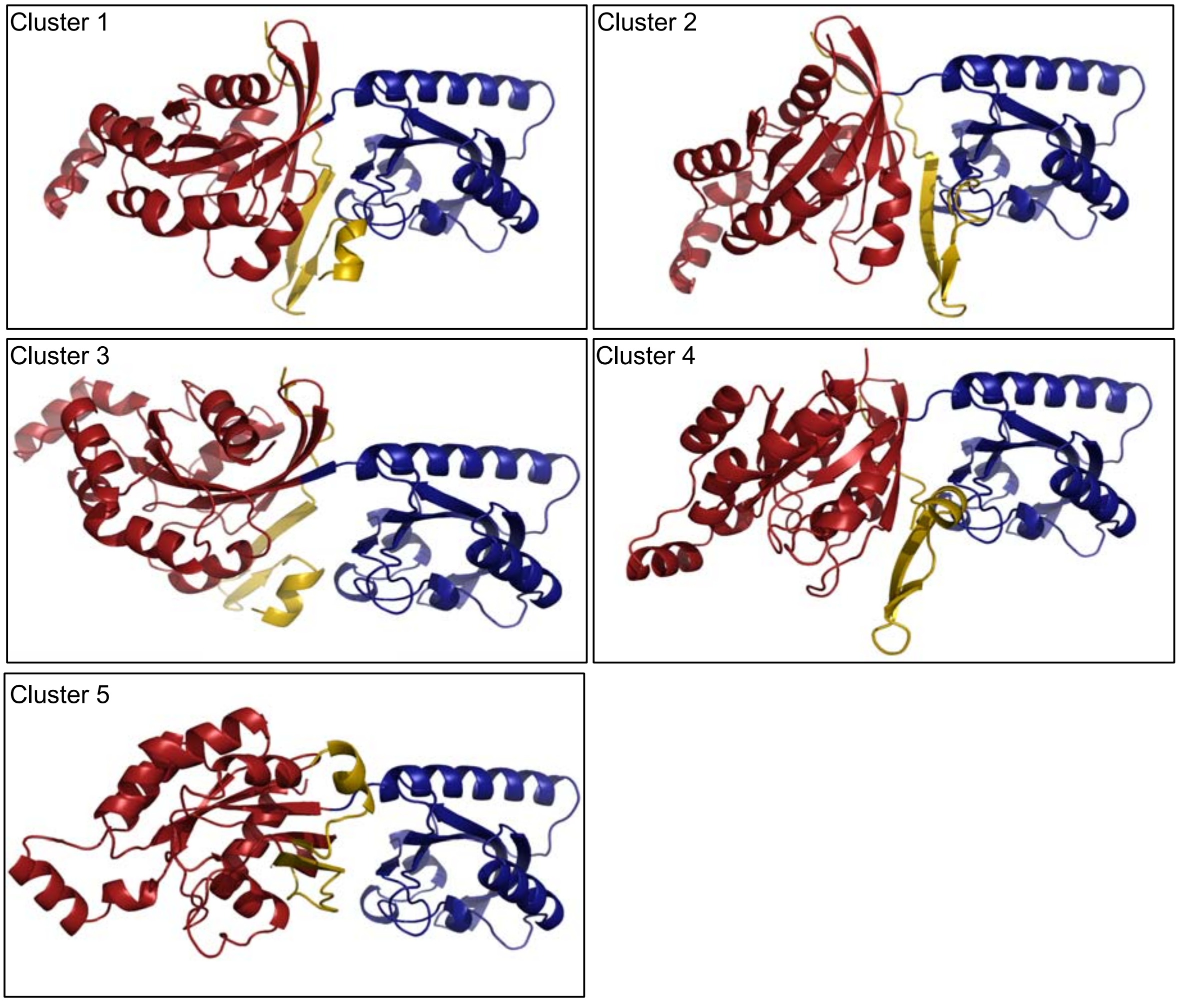

Figure S11. Modelling of the LOV2-Rac1 546-4 construct for CRIB binding. Models of the five most populated clusters obtained for the 546-4 constructs were analysed for their abilities to bind the CRIB domain (see details in method section). Of the 1000 models generated during the simulations, 813 were unable to bind CRIB. The model in the centre of each of these clusters was overlaid with CRIB domain. The RMSD of these centre models to the X-ray structure of PA-Rac1 were shown (Table S4). *Red*, Rac1; *blue*, LOV2; and *yellow*, CRIB.

Table S4. Simulations of LOV2-Rac1 545-4 Construct

Cluster Number	Members	Score[1]	Binds CRIB?
1	553	-509	Yes
2	178	-509	Yes
3	107	-507	Yes
4	46	-508	Yes
5	43	-509	Yes

[1] Average of best 10% scoring decoys

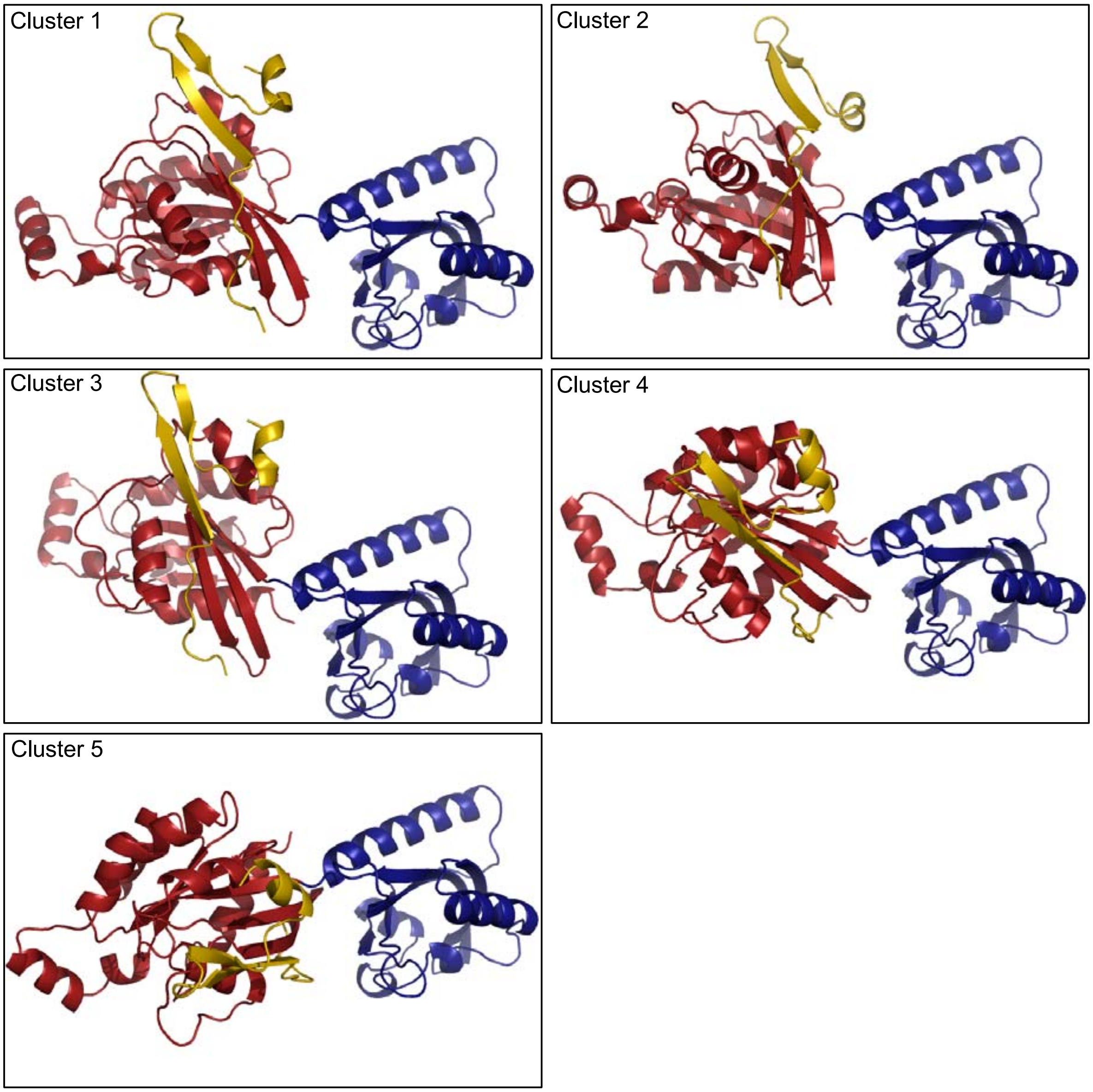

Figure S12. Models of LOV2-Rac1 545-4 construct. Models of the five most populated clusters obtained for the 545-4 constructs were analysed for their abilities to bind the CRIB domain (see details in method section). All 1000 models generated from the simulations were able to bind CRIB. The model in the centre of each of these clusters was overlaid with CRIB domain. The RMSD of these centre models to the X-ray structure of PA-Rac1 were shown (Table S5). *Red*, Rac1; *blue*, LOV2; and *yellow*, CRIB.

Table S5. Simulations of LOV2-Rac1 547-4 Construct

Cluster Number	Members	Score[1]	Binds CRIB?
1	337	-507	Yes
2	115	-500	Yes
3	104	-508	Yes
4	100	-508	Yes
5	63	-491	Yes

[1] Rosetta average score of best 10%

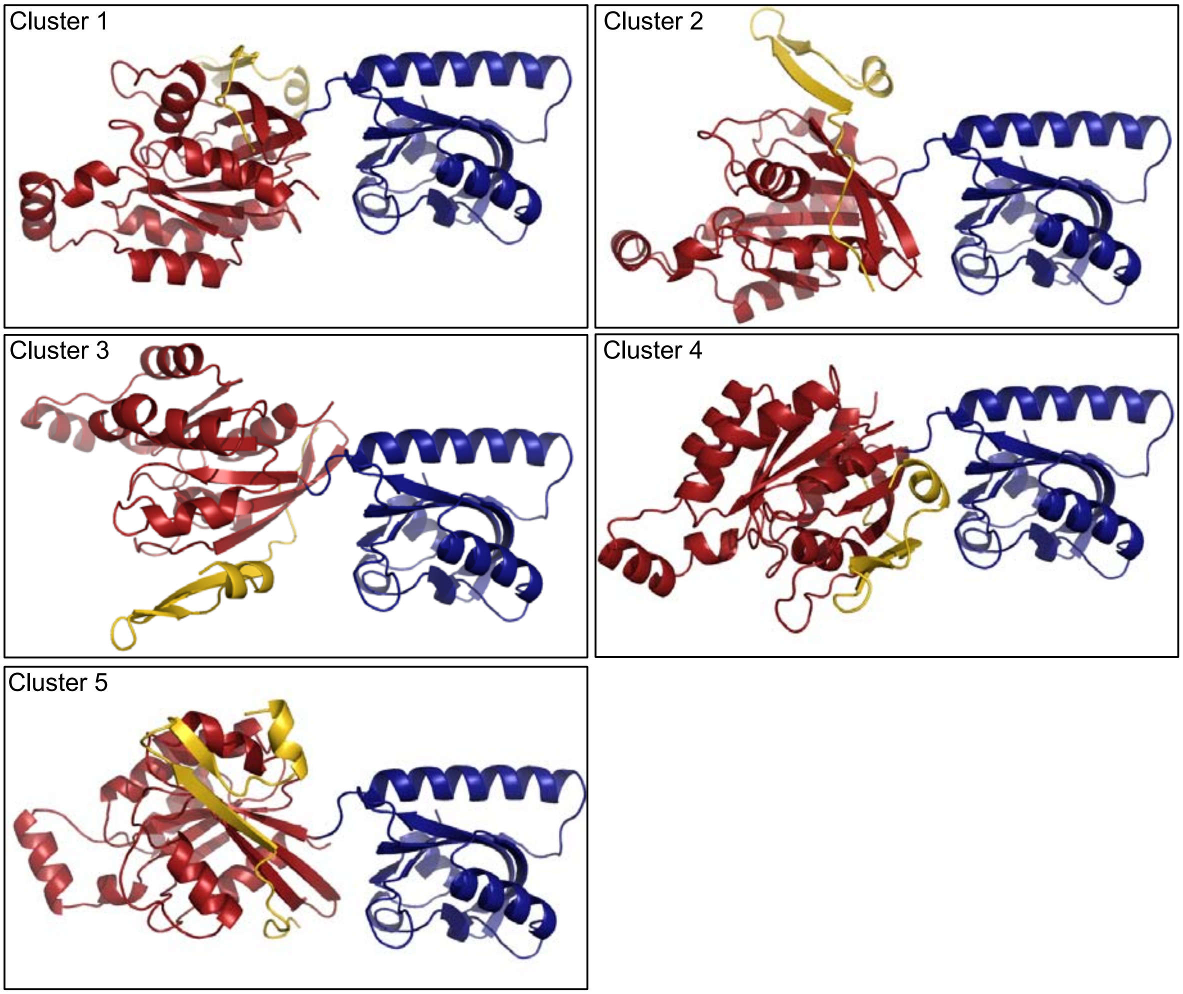

Figure S13. Models of LOV2-Rac1 547-4 construct. Models of the five most populated clusters obtained for the 547-4 constructs were analysed for their abilities to bind the CRIB domain (see details in method section). Of the 1000 models generated during the simulations, 967 were able to bind PAK4 CRIB. The model in the centre of each of these clusters was overlaid with CRIB domain. The RMSD of these centre models to the X-ray structure of PA-Rac1 were shown (Table S6). *Red*, Rac1; *blue*, LOV2; and *yellow*, CRIB.

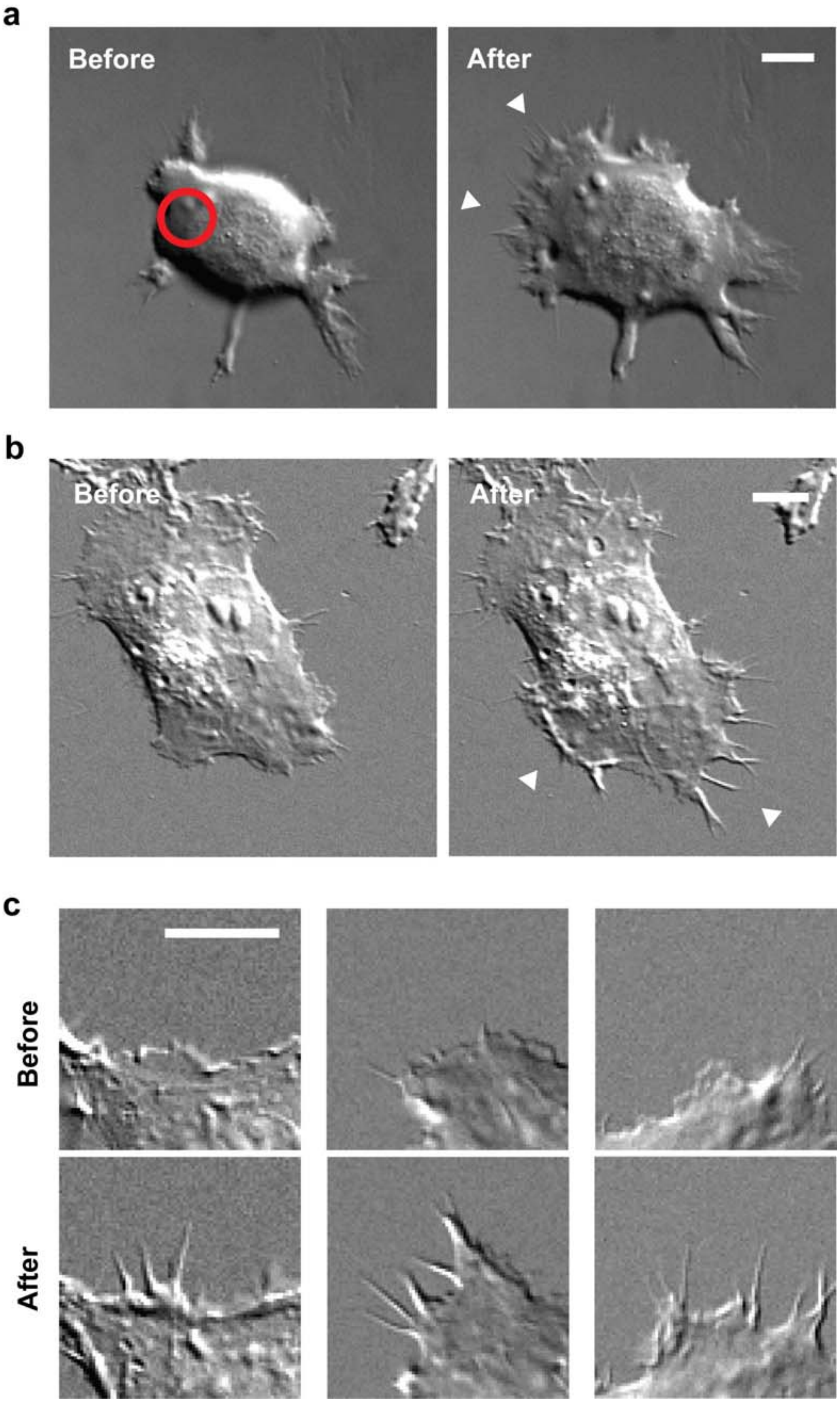
a
Before
After
b
Before
After
c
Before
After

Figure S14. Filopodia and protrusions induced by irradiation of PA-Cdc42 (F56W). **a,** HEK293 cells expressing mCherry-tagged PA-Cdc42-F56W were locally irradiated at 473 nm (red, Ø = 10 µm). DIC images of cells before and after irradiation are shown (filopodia induction in 7 of 7 cells). **b**, HeLa cells expressing mVenus-tagged PA-Cdc42-F56W were globally irradiated with a 100W mercury arc light source (430/24 nm filter, 100 ms at 10 sec intervals for 5 min). DIC images of cells before and after irradiation are shown. Induction of filopodia and/or ruffles was seen in 9 of 9 cells. **c**, Close-ups of changes induced upon irradiation of HeLa cells, including one panel taken from the cell shown in **b** (middle). Arrowheads point to formation of filopodia and ruffles (scale bar = 10 µm). See also Supplementary Movie S16.

LIST OF SUPPLEMENTARY MOVIES

Movie S1 Ruffles and protrusions induced in a HeLa cell expressing PA-Rac1. A HeLa cell transiently expressing mCherry-tagged PA-Rac1 was illuminated throughout the field of view, first with 515 nm light (a wavelength not absorbed by LOV2) then after 5 mins with 458 nm light. Activation of PA-Rac1 at 458 nm led to ruffling and protrusion all around the cell edges. Scale bar is 20 µm.

Movie S2 Localized illumination of PA-Rac1. A serum-starved MEF cell expressing mVenus-tagged PA-Rac1 was irradiated repeatedly (1 minute intervals) in a 20 µm spot with 458 nm light (*red circle*). Initially, localized ruffling was induced by each dose of irradiation. After multiple doses, the cell began to produce a membrane protrusion which grew to 15-µm in length. Unirradiated areas of the cell remained quiescent.

Movie S3 Actin reorganization induced by sequential activation of PA-Rac1 at multiple locations. A HeLa cell co-expressing mVenus-tagged actin and mCherry-tagged PA-Rac1 was sequentially irradiated at four different regions (458 nm, Ø = 20 µm, as shown by fluorescence photobleaching). Protrusion and recovery of actin fluorescence at the leading edge were consistent with Rac1 induction of lamellipodial actin polymerization. (see Supplementary Fig. S5)

Movie S4 Translocation of PAK to protrusions upon PA-Rac1 activation. HeLa cells co-expressing mCerulean-PA-Rac, mVenus-PAK and mCherry (as a volume indicator) were locally irradiated at 473 nm to generate protrusions (red, Ø = 10 µm). Series of ratio images of mVenus-PAK over mCherry before and after irradiation, indicative of the subcellular distribution of PAK, are presented in pseudocolor (ratio).

Movie S5 Reversible induction of ruffling at different locations. A HeLa cell expressing mVenus-tagged PA-Rac1 was sequentially irradiated at two different positions along the cell edge (458nm, Ø = 20 µm, as shown by the bleached regions in the briefly inserted images). The first irradiated region became quiescent as the second pulse caused ruffling elsewhere.

Movie S6 Complex control of cell morphology guided by a moving laser beam. A MEF cell expressing mVenus-tagged PA-Rac1 was exposed to a diffused laser beam at 473 nm, visible due to reflection from the optics. Membrane protrusions and/or ruffles were induced and dissipated in different locations as the beam was moved. Retractions were produced at the side of the cell opposite the site of irradiation.

Movie S7 Diffusion of PA-Rac1 observed using FRAP (fluorescence recovery after photobleaching). A HeLa cell expressing mVenus-tagged PA-Rac1 was photobleached at the spot indicated (*blue*, Ø = 10 µm) with a pulse of 515 nm light. The recovery of mVenus fluorescence (*left*) due to diffusion was followed. *Right*, DIC images.

Movie S8 Diffusion of PA-Rac1 observed using PA-GFP. PA-Rac1 tagged with PA-GFP was activated with a pulse of irradiation at 405 nm in a HeLa cell. The fluorescence of PA-GFP was monitored with 488 nm excitation. *Right*, DIC images. The excitation at 488 nm during image acquisition also caused local PA-Rac1 activation.

Movie S9 Polarization induced by localized activation of PA-Rac1. A MEF cell expressing mVenus-tagged PA-Rac1 was irradiated at 458 nm on one side of the cell (*yellow*, Ø = 10 µm). The pseudocolor map of protrusion (*red*) and retraction (*blue*) indicate polarization of the cell towards the site of PA-Rac1 activation.

Movie S10 Localized irradiation of PA-Rac1-T17N generates reversed polarity. A MEF cell expressing mVenus-tagged PA-Rac1-T17N (dominant negative mutant) was irradiated at 458 nm (yellow, Ø = 10 µm). The cell retracted at the site of irradiation and protruded at the opposite side of the cell, generating polarization away from the site of irradiation.

Movie S11 Irradiation of PA-Rac1-T17N reverses polarization. A MEF cell expressing mVenus-tagged PA-Rac1 was irradiated multiple times at 458 nm on one side of the cell (*yellow*, Ø = 10 μm) where no retraction fibres were seen prior to irradiation. The irradiation produced localized retraction and multiple protrusions elsewhere. Irradiation was shifted to another region of the cell which was actively protruding. This led to a reversal of movement direction, shifting protrusion to retraction. The region that was previously irradiated now began to protrude rather than retract. The pseudocolor map shows protrusion in red and retraction in blue.

Movie S12 Directional migration induced by repeated irradiation at the cell edge. A MEF cell expressing mVenus-tagged PA-Rac1 was repeatedly irradiated at the cell edge (yellow, 49 times, 458 nm, Ø = 10 μm). DIC (*left*) and fluorescence images (*middle*) were acquired at 5 second intervals. The protrusion/retraction map (*right*) indicates polarized movement towards the site of irradiation. *Red,* protrusion; *blue*, retraction.

Movie S13 Directional migration induced by PA-Rac1 in HEK293 cells. A HEK293 cell expressing mCherry-tagged PA-Rac1 was relatively stationary for 5 minutes before irradiation with a 473 nm laser (bright spot in the DIC image) was focused on its cell border. The irradiation induced local lamellipodial protrusion followed by cell movement. (Scale bar = 20 μm).

Movie S14 Downregulation of RhoA activity propagates from the site of PA-Rac1 activation. HeLa cells co-expressing RhoA biosensor and either mCherry-tagged PA-Rac1 or its dark state mutant (C450M) were irradiated at 473 nm (blue spot, Ø = 10 μm). FRET efficiency (E_{corr}) is shown in pseudocolor before and after irradiation (cooler colors indicate RhoA inactivation).

Movie S15 Ruffle translocation upon activation of PA-Rac1. A MEF cell co-expressing the RhoA biosensor and mCherry-tagged PA-Rac1 was continuously irradiated at 473 nm at the cell edge (dotted blue circle). YFP acceptor excitation and emission from the biosensor, displayed in pseudocolor, is used to track ruffles.

Movie S16 Contrasting morphological changes produced by activation of PA-Cdc42 versus PA-Rac1. HeLa cells expressing mVenus-PA-Cdc42 (*left*) or mVenus-PA-Rac1 (*right*) were illuminated with a 100 W mercury arc light source (430/24 nm filter, 100% power x 100 ms every 10 secs). The DIC images before and during illumination (*activation*, *red*) are presented. Arrowheads indicate induction of filopodia (*PA-Cdc42*) or broad protrusions (*PA-Rac1*). Scale bar = 10 μm.

REFERENCES

1 Bystroff, C. & Baker, D. Prediction of local structure in proteins using a library of sequence-structure motifs. *Journal of Molecular Biology* **281**, 565-577, (1998).

2 Nagai, T. *et al.* A variant of yellow fluorescent protein with fast and efficient maturation for cell-biological applications. *Nat Biotechnol* **20**, 87-90, (2002).

3 Shaner, N. C. *et al.* Improved monomeric red, orange and yellow fluorescent proteins derived from Discosoma sp. red fluorescent protein. *Nat Biotechnol* **22**, 1567-1572, (2004).

4 Patterson, G. H. & Lippincott-Schwartz, J. A photoactivatable GFP for selective photolabeling of proteins and cells. *Science* **297**, 1873-1877, (2002).

5 Salomon, M., Christie, J. M., Knieb, E., Lempert, U. & Briggs, W. R. Photochemical and mutational analysis of the FMN-binding domains of the plant blue light receptor, phototropin. *Biochemistry* **39**, 9401-9410, (2000).

6 Kabsch, W. Automatic processing of rotation diffraction data from crystals of initially unknown symmetry and cell constants. *Journal of Applied Crystallography* **26**, 795-800, (1993).

7 McCoy, A. J. *et al.* Phaser crystallographic software. *Journal of Applied Crystallography* **40**, 658-674, (2007).

8 Halavaty, A. S. & Moffat, K. N-and C-Terminal Flanking Regions Modulate Light-Induced Signal Transduction in the LOV2 Domain of the Blue Light Sensor Phototropin 1 from Avena sativa. *Biochemistry* **46**, 14001-14009, (2007).

9 Hirshberg, M., Stockley, R. W., Dodson, G. & Webb, M. R. The crystal structure of human rac1, a member of the rho-family complexed with a GTP analogue. *Nature Structural Biology* **4**, 147-152, (1997).

10 Adams, P. D. *et al.* PHENIX: building new software for automated crystallographic structure determination. *Acta Crystallogr D Biol Crystallogr* **58**, 1948-1954, (2002).

11 Emsley, P. & Cowtan, K. Coot: model-building tools for molecular graphics. *Acta Crystallogr D Biol Crystallogr* **60**, 2126-2132, (2004).

12 Davis, I. W., Murray, L. W., Richardson, J. S. & Richardson, D. C. MOLPROBITY: structure validation and all-atom contact analysis for nucleic acids and their complexes. *Nucleic Acids Research* **32**, W615, (2004).

13 Laskowski, R. A., MacArthur, M. W., Moss, D. S. & Thornton, J. M. PROCHECK: a program to check the stereochemical quality of protein structures. *J. Appl. Cryst.* **26**, 283-291, (1993).

14 Rohl, C. A., Strauss, C. E., Misura, K. M. & Baker, D. Protein structure prediction using Rosetta. *Methods Enzymol* **383**, 66-93, (2004).

15 Das, R. & Baker, D. Macromolecular Modeling with Rosetta. *Annual review of biochemistry*, (2008).

16 Wollacott, A. M., Zanghellini, A., Murphy, P. & Baker, D. Prediction of structures of multidomain proteins from structures of the individual domains. *Protein Science* **16**, 165, (2007).

17 Kuhlman, B. & Baker, D. Native protein sequences are close to optimal for their structures. *Proc Natl Acad Sci U S A* **97**, 10383-10388, (2000).

18 Pertz, O., Hodgson, L., Klemke, R. L. & Hahn, K. M. Spatiotemporal dynamics of RhoA activity in migrating cells. *Nature* **440**, 1069-1072, (2006).

19 Hodgson, L., Pertz, O. & Hahn, K. M. Design and optimization of genetically encoded fluorescent biosensors: GTPase biosensors. *Methods Cell Biol* **85**, 63-81, (2008).

20 Hodgson, L., Shen, F. & Hahn, K. M. Biosensors for characterizing the dynamics of Rho family GTPases in living cells. *Current protocols in cell biology*, (in press).

21 Zal, T. & Gascoigne, N. R. Photobleaching-corrected FRET efficiency imaging of live cells. *Biophys J* **86**, 3923-3939, (2004).

22 Reits, E. A. & Neefjes, J. J. From fixed to FRAP: measuring protein mobility and activity in living cells. *Nat Cell Biol* **3**, E145-147, (2001).

23 Axelrod, D., Koppel, D. E., Schlessinger, J., Elson, E. & Webb, W. W. Mobility measurement by analysis of fluorescence photobleaching recovery kinetics. *Biophys J* **16**, 1055-1069, (1976).

24 Katsumi, A. *et al.* Effects of cell tension on the small GTPase Rac. *J Cell Biol* **158**, 153-164, (2002).

25 Gao, Y., Xing, J., Streuli, M., Leto, T. L. & Zheng, Y. Trp(56) of rac1 specifies interaction with a subset of guanine nucleotide exchange factors. *J Biol Chem* **276**, 47530-47541, (2001).

26 Moissoglu, K., Slepchenko, B. M., Meller, N., Horwitz, A. F. & Schwartz, M. A. In vivo dynamics of Rac-membrane interactions. *Mol Biol Cell* **17**, 2770-2779, (2006).

27 Nassar, N., Hoffman, G. R., Manor, D., Clardy, J. C. & Cerione, R. A. Structures of Cdc42 bound to the active and catalytically compromised forms of Cdc42GAP. *Nature Structural Biology* **5**, 1047-1052, (1998).

28 Rittinger, K., Walker, P. A., Eccleston, J. F., Smerdon, S. J. & Gamblin, S. J. Structure at 1.65 A of RhoA and its GTPase-activating protein in complex with a transition-state analogue. *Nature* **389**, 758-762, (1997).

29 Zhao, Z. S. *et al.* A conserved negative regulatory region in alphaPAK: inhibition of PAK kinases reveals their morphological roles downstream of Cdc42 and Rac1. *Mol Cell Biol* **18**, 2153-2163, (1998).